JOURNAL OF CATALYSIS **158,** 570–582 (1996)
ARTICLE NO. 0055

Photocatalyzed Oxidation of Ethanol and Acetaldehyde in Humidified Air

Michael L. Sauer and David F. Ollis

Department of Chemical Engineering, North Carolina State University, Raleigh, North Carolina 27695-7905

Received February 8, 1995; revised August 2, 1995; accepted August 4, 1995

Photocatalyzed oxidation of ethanol and acetaldehyde in humidified air was carried out to establish a first complete kinetic model for a photocatalyzed multispecies network. Two photocatalysts were examined in a batch, recirculation reactor, near-UV illuminated TiO_2 (anatase) coated (i) on the surface of a nonporous quartz glass plate and (ii) on a porous ceramic honeycomb monolith. The former contained only illuminated (active) surfaces, the latter consisted of substantial "dark" surfaces coated with a thin layer of illuminated (active) catalyst. Ethanol was photooxidized to acetaldehyde and formaldehyde intermediates, and eventually to carbon dioxide and water products. The catalyst and monolith surfaces adsorbed appreciable fractions of the trace ethanol, acetaldehyde, formaldehyde, carbon dioxide, and water present. Ethanol, acetaldehyde, and carbon dioxide adsorption isotherms were measured on both catalysts; the formaldehyde adsorption isotherms were assumed identical to those of acetaldehyde. On the fully illuminated glass plate reactor, all four species were accounted for, and closure of a transient carbon mass balance was demonstrated. Completion of a transient carbon balance on the monolith reactor required inclusion of additional reaction intermediates (acetic and formic acids), which appear to reversibly accumulate on only the dark surfaces. The ethanol and acetaldehyde photocatalyzed oxidation kinetic networks were modeled using Langmuir–Hinshelwood rate forms combined with adsorption isotherms for reactant, intermediates, and product CO_2. For both the quartz plate and monolith catalysts, satisfactory kinetic models were developed to predict the entire time course of ethanol and acetaldehyde multicomponent batch conversions. © 1996 Academic Press, Inc.

1. INTRODUCTION

The photocatalyzed oxidative removal of trace contaminants from air is a growing research area. Gas–solid heterogeneous photocatalytic oxidation of single compound feeds has been previously demonstrated for alkanes (1–6), alcohols (7–12), aldehydes (12–14), ketones (acetone) (12, 15, 16), aromatics (toluene (13, 17), *m*-xylene (12, 14)), halogenates (trichloroethylene (18–29)), and inorganics (ammonia (30)). Photocatalysis is thus established as a potential air treatment and purification technology because of its broad applicability to common, oxidizable air contaminants. Attractive advantages with photocatalysis for air treatment and purification are operation at ambient temperature and pressure (1), use of molecular oxygen as the oxidant (1) and final oxidation products that are usually innocuous (1) (CO_2 and H_2O for the oxidation of small hydrocarbons).

The commercialization prospects for photocatalytic air treatment have recently been discussed by Miller and Fox (31), who estimated the capital and operating costs for treatment of four example contaminated air streams: soil vapor extract (100 ppm TCE), air stripper vent (50 ppm benzene, 250 ppm other VOC), product dryer vent (including 25 ppm methanol, 25 ppm ethanol), and a paint drying vent (10 ppm xylene, odors, plasticizers, surfactants). These example streams of commercial relevance indicate that photocatalytic treatment of air streams containing *several* contaminants may be commonly required. No literature models exist for such streams, so the present work involving a multicomponent oxidation network (ethanol, acetaldehyde, formaldehyde, carbon dioxide, water) was undertaken to provide a basis for photocatalytic network modeling.

This gas–phase ethanol photocatalytic oxidation was recently reported by Wolfrum *et al.* (32), who identified acetaldehyde and formaldehyde as intermediates. A kinetic model was developed assuming a series degradation pathway for ethanol (e.g., ethanol → acetaldehyde → formaldehyde → carbon dioxide) and utilizing Langmuir–Hinshelwood kinetic rate forms. Kinetic parameters for each component were determined separately, and then combined in a kinetic model attempting to predict the kinetics of ethanol degradation. The results showed a shortage in the transient carbon balance at intermediate conversion times. The present study extends and completes these results by (1) incorporating a complete degradation pathway for ethanol photooxidation, (2) including surface adsorption inventories for volatile species to facilitate closure of the carbon mass balance, (3) studying the effect of

0021-9517/96 $12.00

different catalyst supports on the ethanol kinetics, and (4) developing a predictive network kinetic model for ethanol degradation, including all intermediates and products.

Acetaldehyde was examined for two reasons. The first intermediate for ethanol conversion is acetaldehyde, and we use here a fully characterized acetaldehyde photocatalyzed oxidation model to demonstrate subsequently a predictive model for ethanol. Also, both acetaldehyde and formaldehyde are undesired intermediates; they possess lower recommended exposure concentrations than does ethanol (maximum allowable exposure levels: ethanol = 1000 ppm; acetaldehyde = 100 ppm; formaldehyde = 3 ppm (33)). The ability to predict concentrations of such unwelcome aldehydes may be important in designing reactors of size sufficient to convert reactant *and* all problematic intermediates to sufficiently low concentrations.

Earlier work by the automobile industry utilized a honeycomb monolith configuration on a large scale for thermal catalytic converters (34). Central advantages of the monolith configuration are a low pressure drop and a high surface area to volume ratio (34, 35); the low pressure drop allows the force of the exhaust gases from the engine to drive the gas flow through the catalytic reactor with a negligible engine back pressure. The use of a photocatalytic monolith for trace contaminant oxidative removal allows retention of the low pressure drop characteristic of the monolith coupled with the room temperature, low pressure photodestruction of the pollutants (16, 36, 37).

Suzuki *et al.* (Toyota R/D) examined photooxidation of trace odor compounds in air over TiO_2 in the first report of a photocatalytic monolith recirculating batch reactor (13). Acetaldehyde, isobutyric acid, toluene, methylmercaptan, hydrogen sulfide, and trimethylamine were individually converted; disappearance kinetics were fitted with a pseudo-first-order equation, and no intermediates were followed. In a previous paper (16), we described photocatalytic oxidation of acetone, which degraded completely with no kinetically important intermediates detected. A complete *single*-component kinetic model (including rate equation and surface adsorbed inventories) was demonstrated for a TiO_2-coated ceramic honeycomb monolith in a batch recirculating system.

Recent work elucidated the photocatalytic oxidation of another high quantum yield gas-phase contaminant, trichloroethylene (TCE) (24, 28). TCE is photooxidized through a multispecies network including dichloroacetyl chloride, phosgene, carbon monoxide, carbon dioxide, HCl, and molecular chlorine. Several of these intermediates and products pose safety and health concerns. The development of multicomponent kinetic models for conversion of this important chlorinated air contaminant, as accomplished for ethanol in the present paper, would give a predictive basis for a second contaminant class with promising potential for photocatalytic treatment, the chlorinated alkenes.

The present gas–solid photocatalytic *monolith* reactor study was undertaken to demonstrate the utility of the monolith reactor configuration for a more complicated kinetic network. The reactant chosen was ethanol, which generates several kinetically important intermediates (11, 32) enroute to complete oxidation.

The process economics of photocatalytic oxidation depend substantially on the apparent photoefficiency, defined here as molecules of reactant converted per incident photon (31). After trichloroethylene and perchloroethylene, ethanol exhibits one of the highest measured quantum efficiencies in gas–solid photocatalysis (31), leading to its favorable consideration in photocatalyst process economics. Berman *et al.* (38) reported an apparent ethanol quantum efficiency of 190%, while values of 10–30% were observed in the current study. Experiments and a reactor network ethanol model taking into account both adsorption and catalytic kinetics of all species will demonstrate the applicability of the monolith reactor for photocatalytic conversion of this important air contaminant.

2. METHOD

Our reactor system (Fig. 1) incorporates a catalyst support (nonporous quartz glass plate or porous ceramic honeycomb monolith) with titanium dioxide particles coated on the surface. The gas-tight recirculating loop is constructed of 3-in i.d. glass sections and couplings (Ace Glass). In differential conversion operation, the recycle loop and catalyst support act as an ideal stirred tank batch reactor (STBR), maintaining a well-mixed gas volume, since the conversion per pass was $\leq$0.67% for all runs.

The reactor configuration shown provides illumination of the catalyst from light sources located outside of the system. Quartz plate windows allow use of 200–300 nm UV light if desired. The experimental apparatus utilized two 100 W UV medium pressure mercury lamps with a near-UV filter attachment, with one lamp located at each end of the reactor. Recirculation air flow in the system is driven by a 3-in diameter, 24 V DC fan, which provides a maximum recirculation rate of 3.3 CFM, corresponding to a system recirculation time of 11.8 s and a residence time per pass in the monolith of 0.45 s. The gas sampling point in the recycle loop allows periodic monitoring of reactant and product concentrations. All air samples were analyzed by gas chromatography (Perkin–Elmer Sigma Series 1) operating with a flame ionization detector (FID) and an Alltech SS column, with Haysep P 80/100 mesh packing. Carbon dioxide was measured with an infrared gas analyzer (Horiba Model PIR-2000). A hygrometer equipped with a thermocouple was added to the system to measure simultaneously the relative humidity and temperature, from

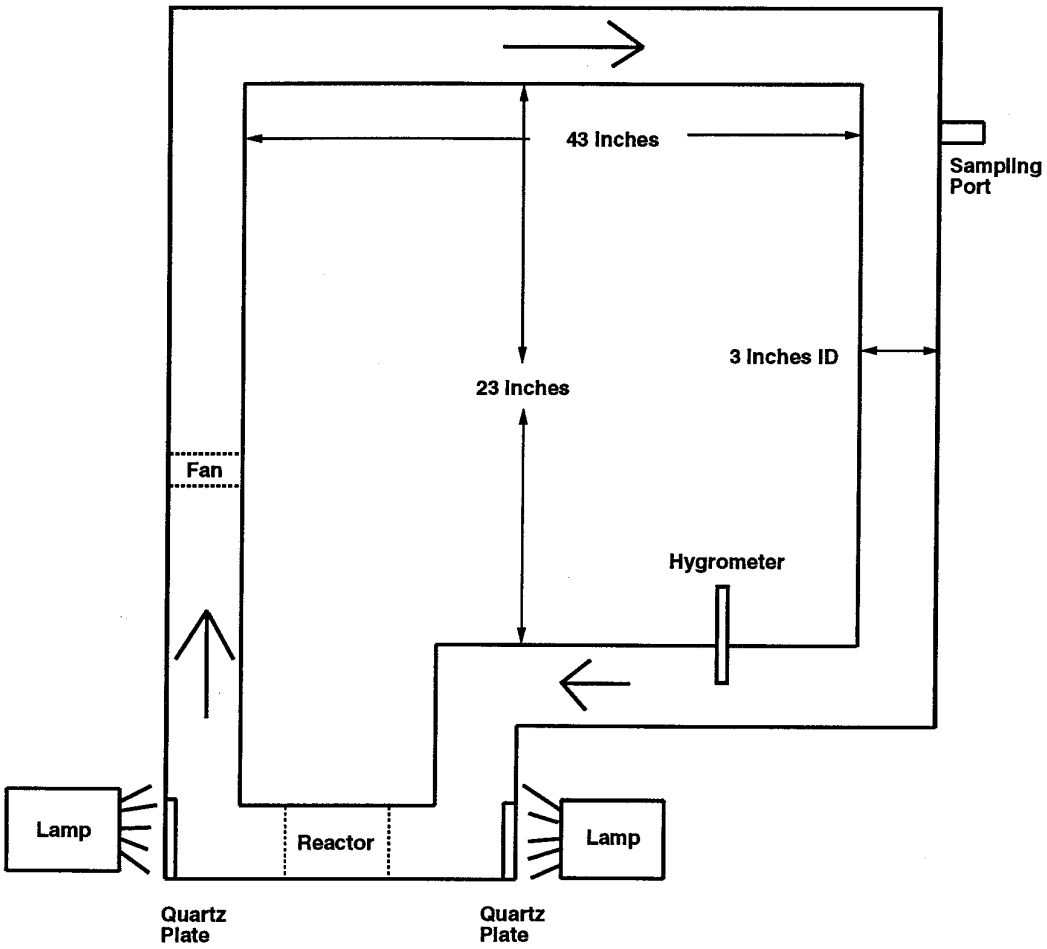

FIG. 1. Experimental photocatalytic reactor system.

which the gas-phase water concentration may be calculated. Finally, a pressure gauge, vacuum port, gas tank inlet feed, and flowrate calibration ports were installed to allow monitoring and safe use of the system.

The catalyst powder was Degussa P25 titanium dioxide, which is mostly anatase with a primary particle diameter of 30 nm and a specific surface area of 50 ± 15 (m^2/g) (Degussa). The P25 particles were spherical and nonporous, with a stated purity of >99.5% TiO_2 (Degussa). Stated impurities include Al_2O_3 (<0.3%), HCl (<0.3%), SiO_2 (<0.2%), and Fe_2O_3 (<0.01%). Five 1.0-cm holes were cut to allow air flow through the 3-in diameter, 0.25-in-thick clear, nonporous quartz glass plate (GM Associates); it was then coated with untreated titanium dioxide powder. The ceramic honeycomb monoliths were obtained from Corning, shaped into 3-in diameter, 6-in-long cylinders, then coated with untreated titanium dioxide powder. These cordierite monoliths had a roughly uniform pore size of about 10 μm and a BET surface area of about 0.4 (m^2/g) (Corning), which for our 325.9 g monolith gave approximately 130 m^2 of internal pore surface area. The monolith used here has square channels of width 0.167 in (Corning), with a total apparent external surface area of 3550 cm^2 for all channels in the 3-in diameter monolith.

The coating of TiO_2 particles on the supports was accomplished by dipping the supports for about 15 s into a well-mixed slurry of 5 wt% TiO_2 in deionized water. The coated support was dried in air for 3–4 h to remove bulk water, leaving a layer of TiO_2 particles on the surface. This coating process was repeated several times, and resulted in deposition of 0.0154 g (quartz plate) and 13.80 g (monolith) of TiO_2 and a surface area of catalyst coating of 0.77 m^2 (quartz plate) and 690 m^2 (monolith). The approximate thickness of the TiO_2 film was 0.5 μm (quartz plate) and 10.1 μm, (monolith), calculated by assuming a nonporous, uniform deposition of crystalline anatase TiO_2 (3.84 (g/cm^3)). Teichner *et al.* have shown that 99% of near-UV light absorption occurs with a 4.5 μm powder layer of TiO_2 (1). Thus, our coating process produced a powder film on the glass in which *all* TiO_2 particles present are illuminated;

and the coated monolith catalyst contains both a thin TiO_2 illuminated layer in all channels and appreciable TiO_2 and honeycomb surface which is not illuminated.

In a typical experiment, the air recirculation is established, and the desired amount of liquid water is injected and allowed to evaporate (aided by a heat gun), circulate, and come to adsorption equilibrium with the catalyst and support. The desired amount of contaminant (ethanol or acetaldehyde) (HPLC grade) is then injected as liquid and allowed to evaporate, circulate, and also reach gas–solid equilibration. The lamps outside the system are turned on to warm up, with care taken to not yet illuminate the catalyst. When a steady-state contaminant gas-phase concentration is reached within the recirculating system, the catalyst is illuminated (≈4.3% of the lamp output reaches the monolith reactor (39)), and the gas-phase is sampled periodically to provide concentration versus time data for reactant, volatile intermediates, and carbon dioxide product. Samples are taken every 10–30 min, depending on the expected run length.

3. RESULTS

We anticipated that the large internal pore surface area of the honeycomb monolith (130 m^2) and TiO_2 catalyst (glass reactor 0.77 m^2; monolith reactor 690 m^2) would lead to significant adsorption of gas-phase species. A major difference between the glass and monolith reactors is the fraction of catalyst which is illuminated (active); the 0.77 m^2 TiO_2 coated on glass is completely active, while the monolith supported TiO_2 has approximately 40 m^2 (4.5 μm depth) active and 650 m^2 inactive (dark). The kinetics of ethanol degradation we established in the glass plate reactor, while the effect of adsorption on substantial, non-illuminated surfaces coupled with an illuminated catalyst was studied in the monolith reactor. The results of the present study include: (i) measurement and modeling of the ethanol, acetaldehyde, and carbon dioxide single-species adsorption isotherms for the glass plate reactor, (ii) measurement of ethanol and acetaldehyde photooxidation kinetics and an initial rate kinetic analysis on each to determine the photocatalytic model parameters (reaction rate and binding constants) for the glass reactor, and (iii) model of the recycle system transient behavior including the reactant, intermediates, and final photooxidation product and comparison of the predictive transient model and experiments for the glass reactor. Adsorption and kinetic measurements and modeling results for the monolith reactor are similarly developed and presented.

3.1. Glass Reactor

3.1.1. Adsorption. The ethanol and acetaldehyde adsorption isotherms were measured individually on the TiO_2-coated glass reactor. Each isotherm was measured at 27°C with a fixed amount (220 mg) of water in the system (≈40% relative humidity). The amounts of ethanol and acetaldehyde adsorbed were each modeled using a Langmuir isotherm,

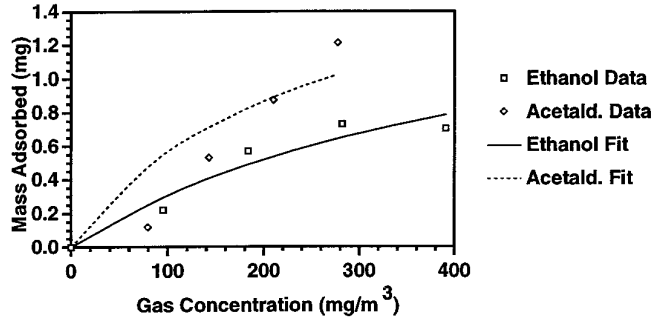

FIG. 2. Adsorption experimental data and model fits for ethanol and acetaldehyde on the TiO_2-coated glass plate using a linear isotherm.

$$M_i^{\text{ads}} = \frac{\mu_i T_i C_i}{1 + T_i C_i} \quad [1]$$

where M_i^{ads} is the mass of i (ethanol, acetaldehyde) adsorbed on the coated glass (mg); μ_i is the maximum number of molecules of i in a monolayer; T_i is the adsorption binding constant for i (m^3/mg); and C_i is the gas-phase concentration of i (mg/m^3).

The constants μ_E, T_E, μ_A, and T_A were determined from the experimental data in Fig. 2; the resulting parameter values are μ_E = 1.7 mg, T_E = 0.0022 (m^3/mg) (r^2 = 0.939) and μ_A = 1.9 mg, T_A = 0.0042 (m^3/mg) (r^2 = 0.914).

The measurement of a formaldehyde isotherm was problematic, so the adsorption constant for formaldehyde was assumed identical to the chemically similar acetaldehyde, thus $\mu_F = \mu_A$ = 1.9 mg and $T_F = T_A$ = 0.0042 (m^3/mg). The fraction of carbon dioxide adsorbed was ≈33% over this same concentration range, corresponding to an adsorption constant T_C = 0.0090 m^3 for a linear isotherm. These adsorption results are used later to obtain a complete carbon mass balance.

3.1.2. Photooxidation. We now describe the ethanol photooxidation kinetic analysis, which involves determination of kinetic parameters and development of a transient model to predict the oxidation network behavior. Figure 3 shows the ethanol degradation pathway through two observed gas-phase intermediates (acetaldehyde and formaldehyde) to the final product (carbon dioxide). The ethanol photocatalytic destruction on the TiO_2 is assumed to follow a single-site Langmuir–Hinshelwood rate form (background oxygen pressure = constant), where the alcohol reactant and partially oxidized intermediates compete for surface sites, thereby inhibiting the photooxidation rates of each other. The simplifying assumption is made

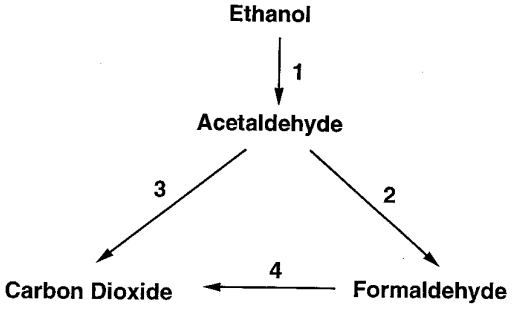

FIG. 3. Ethanol degradation kinetic pathway on the coated glass plate.

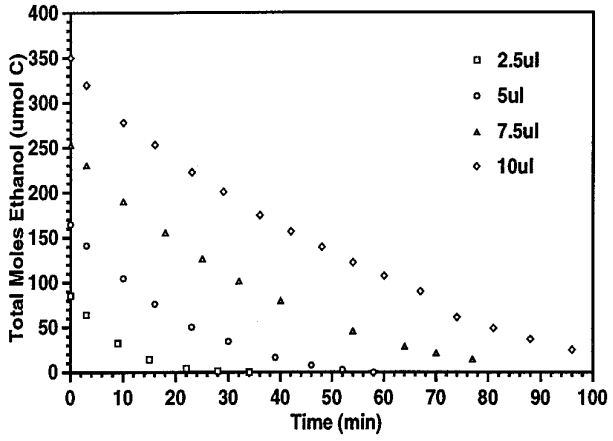

FIG. 4. Ethanol photooxidation experimental data for the coated glass plate, initial concentrations (90 − 400 (mg/m^3)).

that the product (carbon dioxide) does not inhibit the photocatalytic rates. The resulting rate equation for ethanol is

$$r_E = -\frac{k_1 K_E C_E}{1 + K_E C_E + K_A C_A + K_F C_F}, \qquad [2]$$

where r_E is the ethanol reaction rate per volume of active (illuminated) catalyst; k_1 is the ethanol reaction rate constant; and K_i is the binding constant for i. The reaction rate constant depends on the light intensity reaching the catalyst (39),

$$k_{1_0} = \frac{k_1}{I^\alpha}, \qquad [3]$$

where k_{1_0} is the light intensity independent reaction rate constant, k_1 is the reaction rate constant from Eq. [2], I is the light intensity in the catalyst layer, and α can vary from 0.5 (high-intensity light) to 1.0 (low-intensity light). The light intensity varies with depth of catalyst layer for the glass and monolith reactors, and also with axial position in the monolith reactor. For simplicity, the current analysis utilizes only average values (k_1) for the reaction rate constants. The local variation of light intensity within the monolith and catalyst layer are discussed elsewhere (16, 37, 39).

The total (adsorbed and gas-phase) ethanol N_E^{tot} (μmol carbon) in the system at any time is

$$N_E^{tot} = N_E^{ads} + N_E^{gas} = \frac{T_E C_E}{\overline{M_E}} + \frac{V_g C_E}{\overline{M_E}} \qquad [4]$$

where N_E^{ads} is the adsorbed ethanol (μmol carbon); N_E^{gas} is gas-phase ethanol (μmol carbon); V_g is gas-phase volume (18420 cm^3); and $\overline{M_E}$ is the ethanol molecular weight (mg/mmol). A reactant mass balance on ethanol gives

$$\frac{dN_E^{tot}}{dt} = -\frac{A_E V_c^{act} k_1 K_E C_E}{1 + K_E C_E + K_A C_A + K_F C_F}, \qquad [5]$$

where A_E is a conversion constant (μmol carbon/mg ethanol); and V_c^{act} is the active (illuminated) catalyst volume (0.004 cm^3 cat). Rearranging Eq. [5] for initial rate analysis (i.e., $C_A = C_F = 0$; $C_E = C_{E_0}$) gives

$$\left(\frac{-A_E V_c^{act}}{(dN_E^{tot}/dt)}\right)_{|t=0} = \frac{1}{k_1 K_E C_{E|_{t=0}}} + \frac{1}{k_1} = B_{E|_{t=0}} \qquad [6]$$

Figure 4 shows four photodegradation data sets of total moles of ethanol versus time. A plot of the initial rate data as $B_{E|_{t=0}}$ versus $1/C_{E|_{t=0}}$ can be represented by a straight line (Fig. 5), with a linear least-squares fit (solid line, Fig. 5) having a slope of 0.921 (cm^3 cat − min/m^3) and an intercept of 0.0158 (cm^3 cat − min/mg) ($r^2 = 0.73$). From Eq. [6], the slope and intercept are given by

$$\text{slope} = \frac{1}{k_1 K_E} \qquad [7]$$

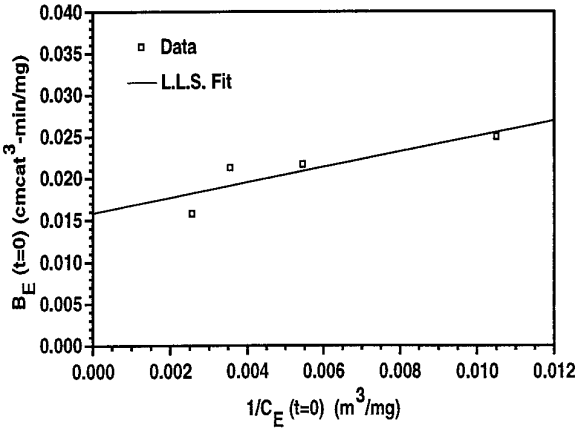

FIG. 5. Initial rate B vs $1/C_0$ for ethanol in the coated glass plate.

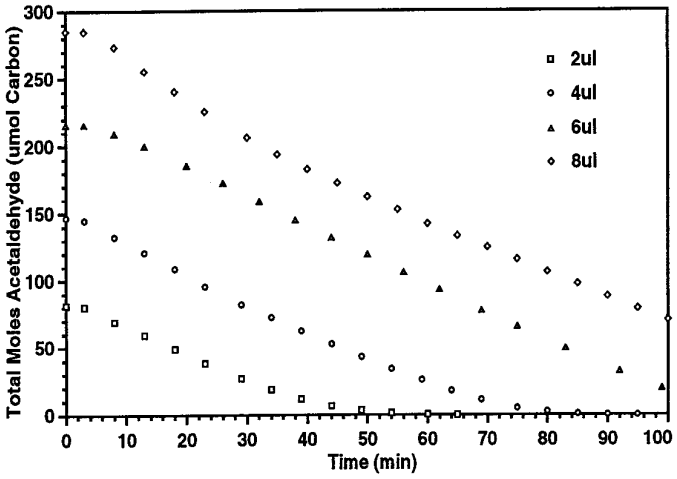

FIG. 6. Acetaldehyde photooxidation experimental data on the coated glass plate, initial concentrations (80 − 330 (mg/m^3)).

$$\text{intercept} = \frac{1}{k_1}. \quad [8]$$

The resultant values for k_1 and K_E are

$$k_1 = 63.1 \frac{\text{mg}}{\text{cm}^3\,\text{cat} - \text{min}} \left(= 0.328 \frac{\text{mg}}{\text{m}^2 - \text{min}} \right) \quad [9]$$

$$K_E = 0.017 \frac{\text{m}^3}{\text{mg}}. \quad [10]$$

For acetaldehyde, the rate form for acetaldehyde formation and disappearance during ethanol oxidation is

$$r_A = \frac{k_1 K_E C_E - (k_2 + k_3) K_A C_A}{1 + K_E C_E + K_A C_A + K_F C_F}. \quad [11]$$

We can determine the reaction rate constants (k_2, k_3) and binding constant (K_A) from experiments with air/acetaldehyde feed. Performing a reactant species mass balance on acetaldehyde gives

$$\frac{dN_A^{tot}}{dt} = - \frac{A_A V_c^{act} (k_2 + k_3) K_A C_A}{1 + K_A C_A + K_F C_F}. \quad [12]$$

Figure 6 shows four experimental data sets of the total moles of acetaldehyde versus time being completely photodegraded by the catalyst. A plot of the initial rate data ($C_E = 0$), analogous to ethanol, can be represented by a straight line (Fig. 7), with a linear least-squares fit (solid line, Fig. 7) having a slope of 2.25 (cm^3 cat − min/m^3) and an intercept of 0.0389 (cm^3 cat − min/mg) ($r^2 = 0.77$). The resulting values of the reaction rate constants (assuming $k_2 = k_3$ as required by network stoichiometry) and binding constant are

$$k_2 = k_3 = 12.8 \frac{\text{mg}}{\text{cm}^3\,\text{cat} - \text{min}} \left(= 0.0665 \frac{\text{mg}}{\text{m}^2 - \text{min}} \right) \quad [13]$$

$$K_A = 0.017 \frac{\text{m}^3}{\text{mg}}. \quad [14]$$

3.1.3. Transient model. The system is treated as a single STBR, assuming that mass transfer effects are negligible, the reaction follows a LH rate form, and the system is well mixed, isothermal and operates under differential conversion conditions (maximum conversion per pass ≈0.67%). The individual species mass balances on reactant ethanol (E), acetaldehyde (A), and formaldehyde (F), intermediates, and final product carbon dioxide (C) are given by the four following coupled differential equations:

$$\frac{dN_E^{tot}}{dt} = - \frac{A_E V_c^{act} k_1 K_E C_E}{1 + K_E C_E + K_A C_A + K_F C_F} \quad [15]$$

$$\frac{dN_A^{tot}}{dt} = \frac{A_E V_c^{act} k_1 K_E C_E - A_A V_c^{act} (k_2 + k_3) K_A C_A}{1 + K_E C_E + K_A C_A + K_F C_F} \quad [16]$$

$$\frac{dN_F^{tot}}{dt} = \frac{A_A V_c^{act} k_2 K_A C_A - A_F V_c^{act} k_4 K_F C_F}{1 + K_E C_E + K_A C_A + K_F C_F} \quad [17]$$

$$\frac{dN_C^{tot}}{dt} = \frac{A_A V_c^{act} k_3 K_A C_A + A_F V_c^{act} k_4 K_F C_F}{1 + K_E C_E + K_A C_A + K_F C_F}. \quad [18]$$

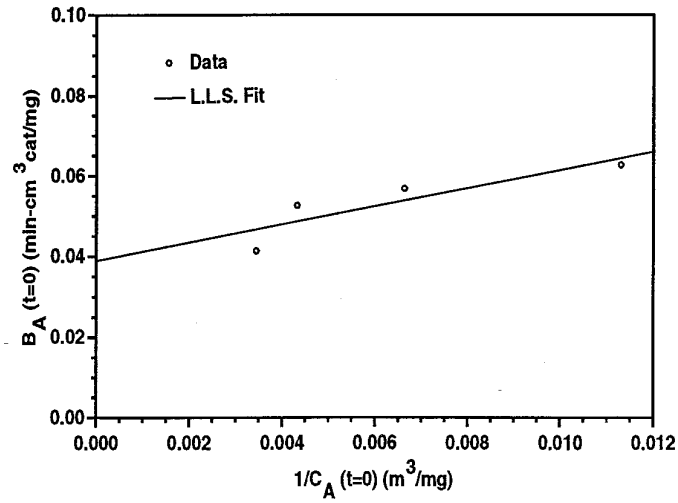

FIG. 7. Initial rate B vs $1/C_0$ for acetaldehyde in the coated glass plate.

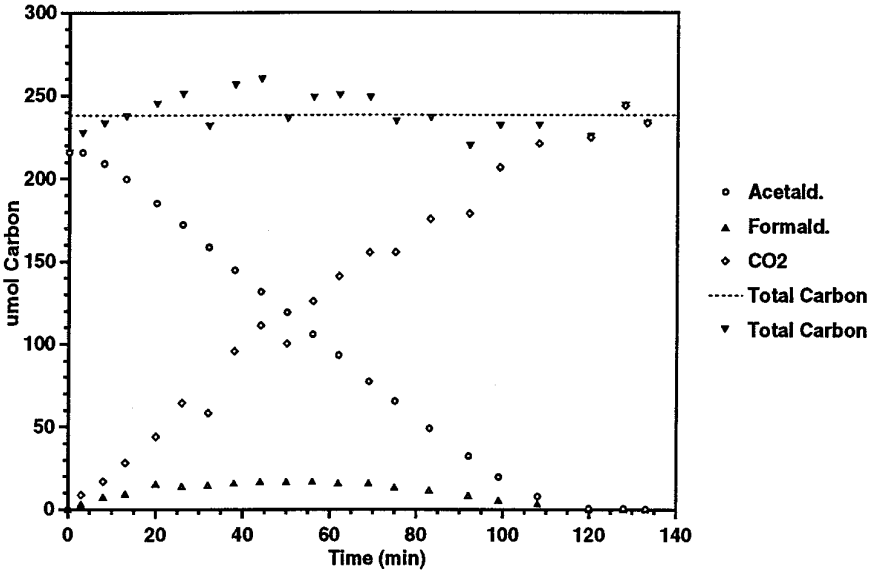

FIG. 8. Acetaldehyde photooxidation experimental data on the coated glass plate, including intermediates, product evolution, and total carbon balance.

All model parameters except k_4 and K_F are known from initial rate data (ethanol, acetaldehyde) or are system constants. The parameters k_4 and K_F were not determined experimentally from formaldehyde feed experiments due to problems associated with generating an air/formaldehyde feed gas reservoir having no other components (e.g., methanol stabilizer). (We were able however, to conveniently analyze formaldehyde as an intermediate in ethanol and acetaldehyde experiments). These two constants are determined using a trial and error analysis on a set of acetaldehyde conversion data. This data (Fig. 8) shows the degradation of acetaldehyde followed by the formation and disappearance of formaldehyde intermediate and eventual complete conversion to carbon dioxide. Figure 8 also shows the experimental closure of the total carbon balance (inverted triangles) as a function of time. Solving Eqs. 16–18 numerically, using all other previously determined parameters and a trial and error analysis for k_4 and K_F under the same conditions as in Fig. 8, gives $k_4 = 40.0$ (mg/cm^3 cat $-$ min) ($= 0.208$ (mg/m^2 $-$ min)) and $K_F = 0.04$ (m^3/mg). The model fit is compared to the experimental data in Fig. 9.

The ethanol oxidation network in Fig. 3 is described by Eqs. [15–18]. We note that the ethanol kinetic parameters (k_1, K_E) are now known from ethanol initial-rate data (no other components present) and the adsorption isotherm is also known (Eq. [1]). Also, the acetaldehyde, formaldehyde, and carbon dioxide model parameters are known from the previous acetaldehyde/air feed experiments. Equations [15–18] should now constitute a *predictive* model for ethanol oxidation over a time course where multiple contaminants (ethanol, acetaldehyde, formaldehyde) are present. To test this hypothesis, the model was evaluated at the same conditions as one of the ethanol experiments; the model predictions and the experiments are compared in Fig. 10. We find the predictive model to give reasonable to excellent agreement for total moles N_i versus time for each species i over all degrees of conversion, including the overall carbon mass balance for ethanol feed concentrations of $90 - 400$ (mg/m^3).

3.2. Monolith Reactor

3.2.1. Adsorption. The ethanol and acetaldehyde adsorption isotherms were measured individually on the catalyst coated monolith. Each isotherm was measured at 27°C with 400 mg (≈40% relative humidity) water in the system. The fractions of ethanol and acetaldehyde adsorbed were relatively high (82–86% ethanol; 38–41% acetaldehyde) and were each modeled using a Langmuir isotherm,

$$M_i^{\text{ads}} = \frac{\mu_i T_i C_i}{1 + T_i C_i}, \qquad [19]$$

where μ_i is the maximum number of molecules of i (ethanol, acetaldehyde) in a monolayer and T_i is the adsorption constant for i (m^3/mg).

The constants μ_E, T_E, μ_A, and T_A were determined from data in Fig. 11, providing parameter values of $\mu_E = 56.0$ mg, $T_E = 0.0028$ (m^3/mg), $R^2 = 0.983$, and $\mu_A = 26.0$ mg, $T_A = 0.0005$ (m^3/mg), $R^2 = 0.985$.

The adsorption constants for formaldehyde were as-

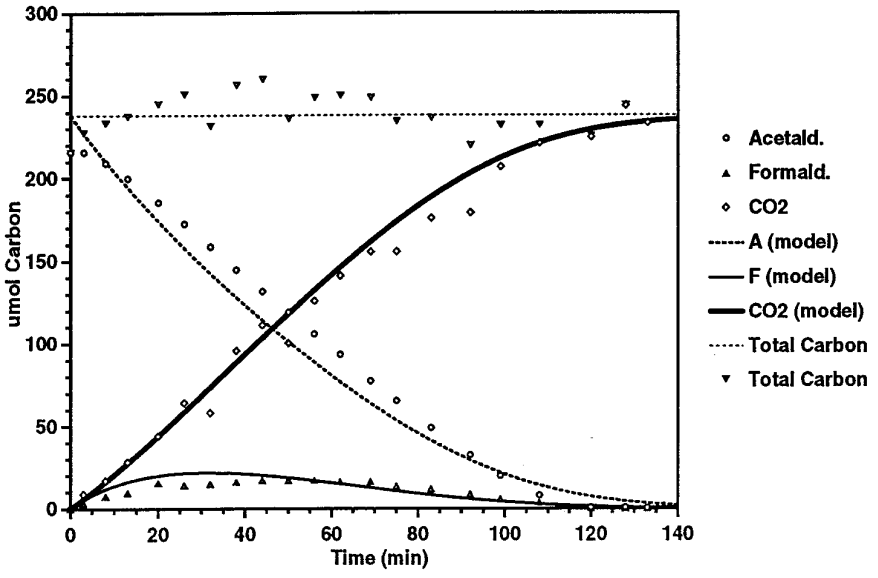

FIG. 9. Model of the full transient system coated glass plate behavior for acetaldehyde.

sumed equal to those for acetaldehyde (as before), thus $\mu_F = \mu_A = 26.0$ mg, $T_F = T_A = 0.0005$ (m^3/mg). The fraction of carbon dioxide adsorbed was ≈12%, and the calculated adsorption constant was $T_C = 0.002$ m^3, assuming a linear isotherm again.

3.2.2. Photooxidation. An attempt to develop an ethanol kinetic model, as above, failed due to incomplete closure of the carbon balance at intermediate to late stages of ethanol conversions. This failure suggested accumulation, on the dark surfaces, of one or more intermediates which were not important in a system with a fully illuminated surface (Fig. 3 network). Acetic acid and formic acid were added to give a larger oxidation network (Fig. 12) for the following reasons: (1) a much better carbon balance closure was obtained, (2) the formaldehyde experimental peak was bimodal, suggesting production from two different sources (e.g., acetaldehyde and acetic acid), (3) the absence of these species from the Fig. 3 network is consistent with the expectation that on an illuminated photocata-

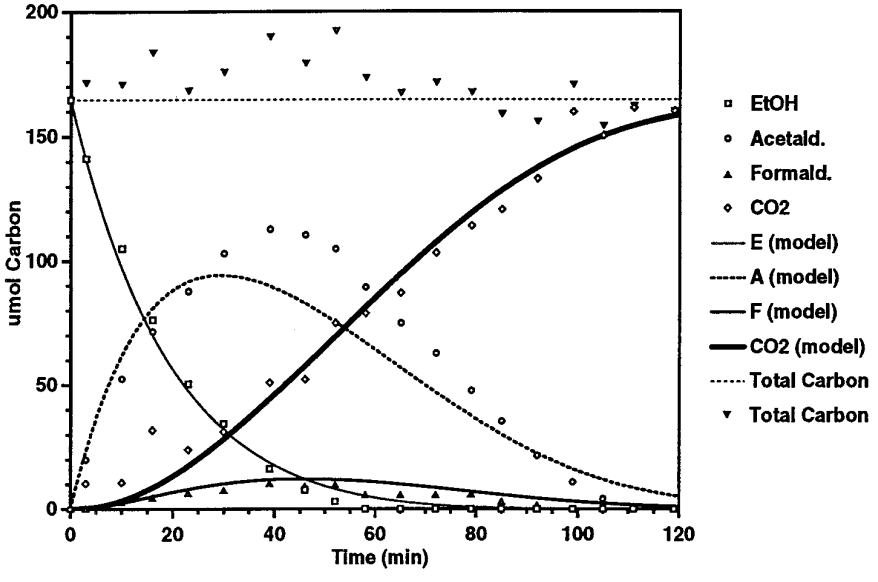

FIG. 10. Predictive model of the full transient system coated glass plate behavior for ethanol.

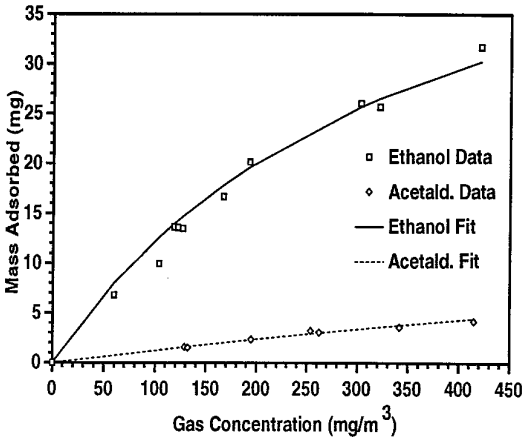

FIG. 11. Adsorption experimental data and model fits for ethanol and acetaldehyde on the TiO_2-coated monolith using a Langmuir isotherm.

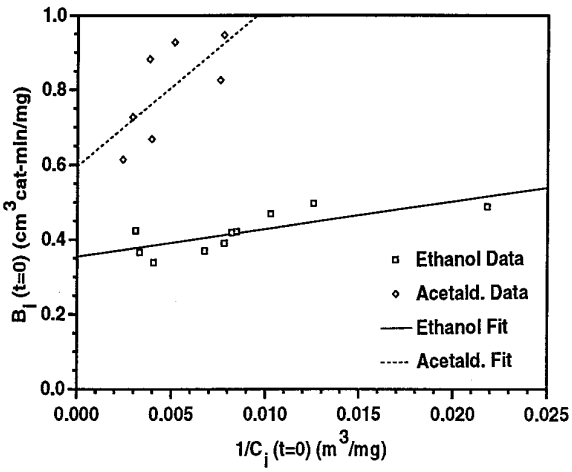

FIG. 13. Initial rate B vs $1/C_0$ for ethanol and acetaldehyde in the monolith reactor.

lyst surface, carboxylic acids would rapidly convert to RCOO·, which would decarboxylate to yield CO_2 + R· (40), and (4) Wolfrum *et al.* (41) have identified formaldehyde and formic acid intermediates (via FTIR) and acetic acid (by gas chromatography) during gas-phase ethanol photocatalytic oxidation. These identified acid species should not accumulate and become kinetically important in the glass plate reactor. On the monolith, however, most of the surface is not illuminated, and trace carboxylic acid intermediates may desorb from illuminated TiO_2 and accumulate reversibly on dark surfaces.

We now develop the ethanol photooxidation kinetic analysis for the expanded ethanol degradation pathway (Fig. 12), which proceeds through four kinetically significant intermediates (acetaldehyde, acetic acid, formaldehyde, and formic acid) to the final product (carbon dioxide). The ethanol photocatalytic destruction on the TiO_2-coated monolith again follows a single-site Langmuir–Hinshelwood rate form, where the oxidation of intermediates competes with the photooxidation of ethanol. The mass balance closure for the glass plate results suggests that acetic acid and formic acid are rapidly converted on illuminated TiO_2 and therefore do not accumulate to inhibit ethanol or other intermediates. The resulting rate form is

$$-r_{\mathrm{E}} = \frac{k_1 K_{\mathrm{E}} C_{\mathrm{E}}}{1 + \sum K_i C_i} \qquad [20]$$

where $\sum K_i C_i = K_{\mathrm{E}} C_{\mathrm{E}} + K_{\mathrm{A}} C_{\mathrm{A}} + K_{\mathrm{F}} C_{\mathrm{F}}$. The species mass balance on ethanol gives

$$\frac{dN_{\mathrm{E}}^{\mathrm{tot}}}{dt} = -\frac{A_{\mathrm{E}} V_{\mathrm{c}}^{\mathrm{act}} k_1 K_{\mathrm{E}} C_{\mathrm{E}}}{1 + \sum K_i C_i}, \qquad [21]$$

where $V_{\mathrm{c}}^{\mathrm{act}}$ is 0.20 cm^3 cat. Rearranging Eq. [21] at initial time again gives Eq. [6].

Ten experimental runs were performed measuring the total moles of ethanol degraded versus time. A plot of the initial rate data as $B_{\mathrm{E}|_{t=0}}$ versus $1/C_{\mathrm{E}|_{t=0}}$ can be represented by a straight line (Fig. 13), with a linear least-squares fit (solid line, Fig. 13) having a slope of 7.37 (cm^3 cat − min/m^3) and an intercept of 0.355 (cm^3 cat − min/mg) ($r^2 = 0.58$). The resultant values for k_1 and K_{E} are

$$k_1 = 2.82 \frac{\mathrm{mg}}{\mathrm{cm}^3\,\mathrm{cat} - \mathrm{min}} \left(= 0.0141 \frac{\mathrm{mg}}{\mathrm{m}^2 - \mathrm{min}} \right) \qquad [22]$$

$$K_{\mathrm{E}} = 0.048 \frac{\mathrm{m}^3}{\mathrm{mg}}. \qquad [23]$$

We next consider the reaction rate constants (k_2, k_7, k_8) and binding constant (K_{A}) for acetaldehyde photooxida-

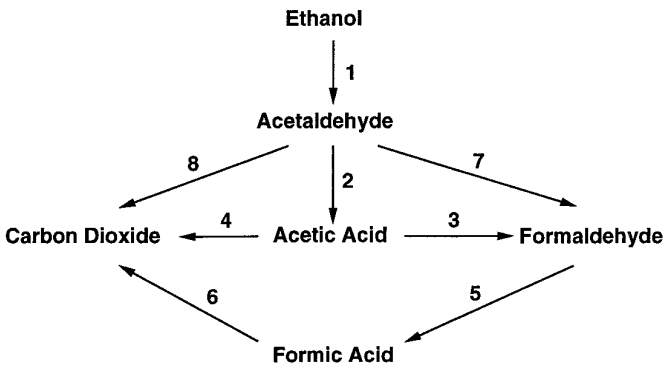

FIG. 12. Ethanol degradation kinetic pathway for the monolith reactor.

tion. The rate form for acetaldehyde production from ethanol and consumption is

$$r_A = \frac{k_1 K_E C_E - (k_2 + k_7 + k_8) K_A C_A}{1 + \sum K_i C_i}. \quad [24]$$

An acetaldehyde mass balance for an air/acetaldehyde feed gives

$$\frac{dN_A^{tot}}{dt} = -\frac{A_A V_c^{act} (k_2 + k_7 + k_8) K_A C_A}{1 + \sum K_i C_i}. \quad [25]$$

Seven experimental runs measuring the total moles of acetaldehyde versus time were executed. A plot of the initial rate data, analogous to ethanol, can be represented by a straight line (Fig. 13), with a linear least-squares fit (dotted line, Fig. 13) having a slope of 42.4 (cm^3 cat $-$ min/m^3) and an intercept of 0.60 (cm^3 cat $-$ min/mg) ($r^2 = 0.48$). The resulting values of the reaction rate constants (assuming $k_2 = k_7 + k_8$ and $k_7 = k_8$) and binding constant are

$$k_2 = 0.84 \frac{mg}{cm^3\ cat - min} \left(= 0.0042 \frac{mg}{m^2 - min} \right) \quad [26]$$

$$k_7 = k_8 = 0.42 \frac{mg}{cm^3\ cat - min} \left(= 0.0021 \frac{mg}{m^2 - min} \right) \quad [27]$$

$$K_A = 0.014 \frac{m^3}{mg}. \quad [28]$$

3.2.3. Transient model. The system is treated as a single STBR, as before. Performing an overall mass balance on the reactant, intermediates, and final product gives the following set of six coupled differential equations (one for each species):

$$\frac{dN_E^{tot}}{dt} = -\left[\frac{A_E k_1 K_E C_E}{1 + \sum K_i C_i} \right] V_c^{act} \quad [29]$$

$$\frac{dN_A^{tot}}{dt} = \left[\frac{A_E k_1 K_E C_E - A_A (k_2 + k_7 + k_8) K_A C_A}{1 + \sum K_i C_i} \right] V_c^{act} \quad [30]$$

$$\frac{dN_{AA}^{tot}}{dt} = \left[\frac{A_A k_2 K_A C_A - A_{AA} (k_3 + k_4) \overline{K_{AA} C_{AA}}}{1 + \sum K_i C_i} \right] V_c^{act} \quad [31]$$

$$\frac{dN_F^{tot}}{dt} = \left[\left(\frac{A_A k_7 K_A C_A}{1 + \sum K_i C_i} \right) + \left(\frac{A_{AA} k_3 \overline{K_{AA} C_{AA}}}{1 + \sum K_i C_i} \right) - \left(\frac{A_F k_5 K_F C_F}{1 + \sum K_i C_i} \right) \right] V_c^{act} \quad [32]$$

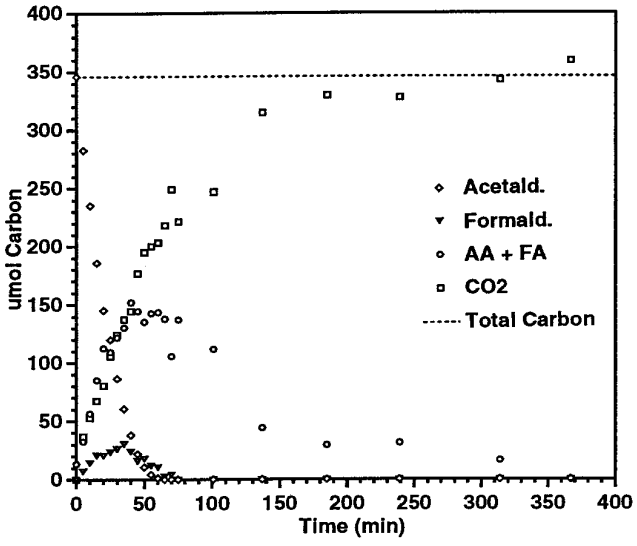

FIG. 14. Acetaldehyde photooxidation experimental data on the monolith reactor, including intermediates and product evolution.

$$\frac{dN_{FA}^{tot}}{dt} = \left[\frac{A_F k_5 K_F C_F - A_{FA} k_6 \overline{K_{FA} C_{FA}}}{1 + \sum K_i C_i} \right] V_c^{act} \quad [33]$$

$$\frac{dN_C^{tot}}{dt} = \left[\left(\frac{A_A V_c^{act} k_8 K_A C_A}{1 + \sum K_i C_i} \right) + \left(\frac{A_{AA} V_c^{act} k_4 \overline{K_{AA} C_{AA}}}{1 + \sum K_i C_i} \right) + \left(\frac{A_{FA} V_c^{act} k_6 \overline{K_{FA} C_{FA}}}{1 + \sum K_i C_i} \right) \right] V_c^{act}. \quad [34]$$

The model parameters k_3, k_4, k_5, k_6, $\overline{K_{AA}}$, K_F, $\overline{K_{AA}}$, are not known and will be determined using a trial and error analysis on a set of acetaldehyde experimental data coupled with the simplifying assumptions that $k_3 = k_4$, $K_F = K_A$, and $\overline{K_{AA}} = \overline{K_{FA}}$. This data set (Fig. 14) shows the degradation of acetaldehyde to a formaldehyde intermediate and eventually complete conversion to carbon dioxide. The shortage in the measured carbon mass balance is calculated at each time as the combination of (nonvolatile) acetic acid and formic acid; these presumed intermediates were not detected on our GC column during any experiments. We solved Eqs. [30–34] numerically as a function of time using the previously determined parameters with a trial and error analysis to determine the four unknown parameter values (k_3, k_5, k_6, $\overline{K_{AA}}$) and the same conditions as in Fig. 14. The final model fit compared to experimental data is shown in Fig. 15 with the resulting values of $k_3 = k_4 = 4.0$ (mg/cm^3 cat $-$ min) $= 0.02$ (mg/m^2 $-$ min), $k_5 = 4.0$ (mg/cm^3 cat $-$ min) $= 0.02$ (mg/m^2 $-$ min),

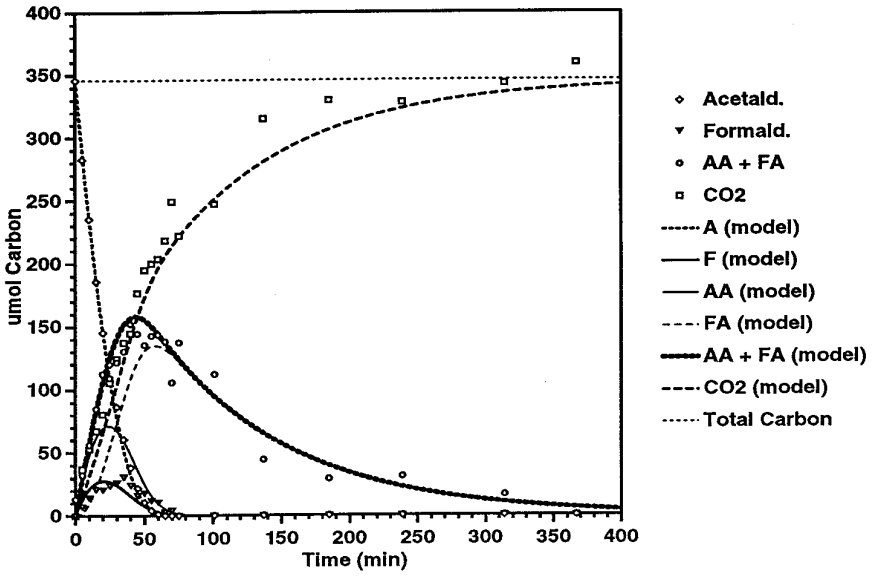

FIG. 15. Model of the full transient system monolith reactor behavior for acetaldehyde.

k_6 = 0.65 (mg/cm^3 cat − min) = 0.0033 (mg/m^2 − min), $\overline{K_{AA}} = \overline{K_{FA}}$ = 65.0 (m^2/mg), and K_F = 0.014 (m^3/mg).

For ethanol again, the model parameters were evaluated from ethanol initial rate data and from acetaldehyde transient data. The full ethanol model (Eqs. [29–34]) should again be predictive for all reaction times for all species (reactant, intermediate, and product). The model was found satisfactory for all ethanol feed concentrations examined (65–370 (mg/m^3)), after adjusting k_6 from 0.65 to 0.40 (mg/cm^3 cat − min). This adjusted model and a full transient experiment are compared in Fig. 16. The alteration of k_6 shifts CO_2 evolution toward longer times, in agreement with the observed data.

4. DISCUSSION

The ethanol photocatalytic oxidation results in the recirculating system were different for the glass plate and monolith reactors. All catalyst on the coated glass plate was active (illuminated), whereas the catalyst-coated monolith had both active (illuminated) and inactive (dark) surface regions. The calculated transient carbon mass balance was

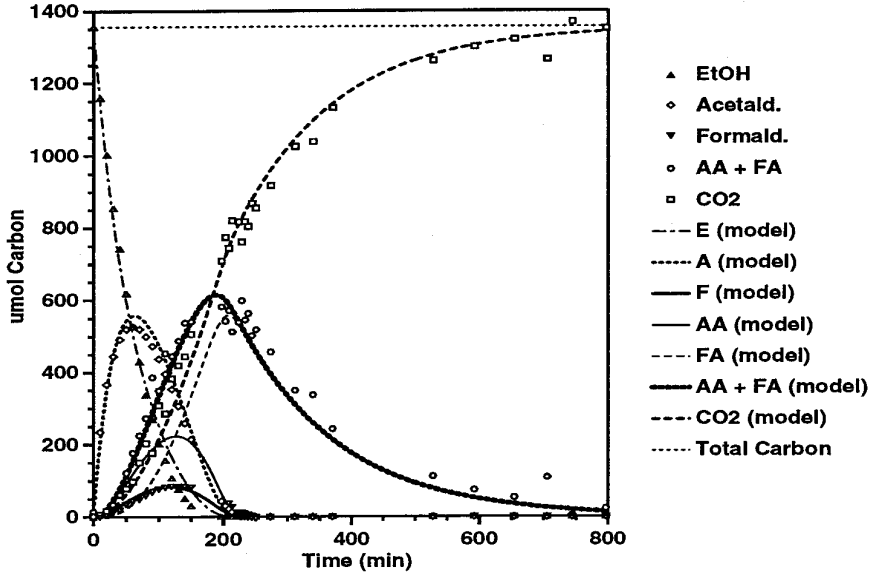

FIG. 16. Predictive model of the full transient system monolith reactor behavior for ethanol.

reasonably closed on the glass reactor, and no surface accumulations of carboxylate species (acetic acid or formic acid) were needed in this model for a fully illuminated surface. In contrast, the monolith reactor mass balance showed at intermediate times a significant carbon deficit, which was modeled as a combination of acetic acid and formic acid intermediates reversibly adsorbed on the (dark) surfaces. Complete evolution of carbon dioxide occurred for the glass plate system as soon as the oxidizable gas-phase species disappeared. For the monolith reactor, a significant lag time occurred between the disappearance of easily measured gas-phase intermediates and the formation of stoichiometric amounts of carbon dioxide. Anderson *et al.* (25) reported evolution of CO_2 from UV-illuminated TiO_2 pellets (these would have some dark surfaces), which had been used previously to degrade TCE, while feeding a gas stream containing only air and water vapor. They state that the CO_2 evolution resulted from photodegradation of adsorbed intermediates which accumulated on the catalyst.

The difference in CO_2 evolution patterns for our two reactors was caused presumably by rapid conversion of acetic and formic acid on the active glass plate catalyst, while the dark surface regions on the monolith allowed reversible accumulation of such acid intermediates; the eventual desorption of the acid intermediates and their readsorption and oxidation on illuminated catalyst is demonstrated by the eventual achievement of 100% carbon balance as CO_2.

Photocatalysis network models have been used in the liquid phase for single and multicomponent feeds (42, 43). Pruden and Ollis (42) measured the complete mineralization of trichloroethylene through a dichloroacetaldehyde intermediate to HCl and CO_2. They used a simple Langmuirian rate equation to satisfactorily represent the reactant initial disappearance, intermediate formation, and HCl product inhibition effects on the conversions. Turchi and Ollis (43) developed from single-component rate equations a network kinetic model for an aqueous mixed feed of benzene and perchloroethylene (PCE). The Langmuir–Hinshelwood (LH) rate equation for PCE gave reasonable agreement with the PCE single-contaminant feed results assuming no kinetically important intermediates, while benzene single feeds were modeled successfully assuming two intermediates. Next, they derived a two-component LH rate form using the single component kinetic constants. Comparing the model to mixed-feed experimental data showed that the model gave reasonable conversion vs time results for benzene and CO_2, but somewhat overpredicted the PCE reaction rate. These liquid-phase network modeling examples, along with the present gas-phase study, show how including all kinetically important intermediates, reactants, and products into transient models can lead to useful predictions for multicomponent systems.

5. CONCLUSIONS

Ethanol (65–410 (mg/m^3) and acetaldehyde-contaminated air streams were treated in a recirculating photoreactor system utilizing near-UV illuminated TiO_2. The TiO_2 was supported on a quartz glass plate (100% active catalyst) and on a ceramic honeycomb monolith (3.5% active catalyst). Kinetic models, assuming competitive Langmuir–Hinshelwood rate forms for ethanol degradation, were developed for both the glass and monolith reactors, incorporating acetaldehyde, formaldehyde, acetic acid (monolith only), and formic acid (monolith only) intermediates and CO_2 product. The adsorption isotherms of all gas-phase species were measured and incorporated into the model, resulting in closure of the total carbon balance on the glass plate reactor. Carbon mass balance closure on the monolith required inclusion of presumed carboxylic acid intermediates, the kinetic constants for which could be evaluated from acetaldehyde transient data. The resulting models were predictive for ethanol feeds for the full transient behavior of both the glass plate and the monolith reactor systems at all ethanol conversions.

ACKNOWLEDGMENTS

This work was supported by a Hoechst-Celanese Kenan Fellowship for Environmental Science and Technology.

REFERENCES

1. Formenti, M., Juillet, F., Meriaudeau, P., and Teichner, S. J., *Chem. Tech.* **1,** 680–686 (1971).
2. Djeghri, N., Formenti, M., Juillet, F., and Teichner, S. J., *Faraday Disc. Chem. Soc.* **58,** 185–193 (1974).
3. Herrmann, J. M., Disdier, J., Mozzanega, M.-N., and Pichat, P., *J. Catal.* **60,** 369–377 (1979).
4. Djeghri, N., and Teichner, S. J., *J. Catal.* **62,** 99–106 (1980).
5. Teichner, S. J., and Formenti, M., *in* "Photoelectrochemistry, Photocatalysis and Photoreactors" pp. 457–489. Reidel, Dordrecht, 1985.
6. Gratzel, M., Thampi, K. R., and Kiwi, J., *J. Phys. Chem.,* **93,** 4128–4132 (1989).
7. Bickley, R. I., Munuera, G., and Stone, F. S., *J. Catal.* **31,** 398–407 (1973).
8. Walker, A., Formenti, M., Meriaudeau, P., and Teichner, S. J., *J. Catal.* **50,** 237–243 (1977).
9. Cunningham, J., and Hodnett, B. K., *J. Chem. Soc. Faraday Trans. 1* **77,** 2777–2801 (1981).
10. Pichat, P., Courbon, H., Disdier, J., Mozzanega, M.-N., and Herrmann, J.-M., *in* New Horizons in Catalysis, pp. 1498–1499. Elsevier, Amsterdam, 1981.
11. Blake, N. R., and Griffin, G. L., *J. Phys. Chem.* **92**(20), 5697–5701 (1988).
12. Peral, J., and Ollis, D. F., *J. Catal.* **136,** 554–565 (1992).
13. Suzuki, K., Satoh, S., and Yoshida, T., *Denki Kagaku* **59**(6), 521–523 (1991).
14. Suzuki, K., *in* "Proceedings, First International Conference on TiO_2 Photocatalytic Purification and Treatment of Water and Air, London, Ontario, Canada, 8–13 Nov. 1992" (D. F. Ollis and H. Al-Ekabi, Eds.), pp. 421–434. Elsevier, Amsterdam, 1993.

15. Raupp, G. B., and Junio, C. T., *Appl. Surf. Sci.* **72,** 321–327 (1993).
16. Sauer, M. L., and Ollis, D. F., *J. Catal.* **149,** 81–91 (1994).
17. Ibusuki, T., and Takeuchi, K., *Atmos. Environ.* **20**(9), 1711–1715 (1986).
18. Dibble, L. A., and Raupp, G. B., in "Proceedings, Arizona Hydrological Society, First Annual Symposium, September 16–17, Phoenix, Arizona, 1988" pp. 221–229, 1988.
19. Dibble, L. A., Ph.D. thesis, Arizona State University, 1989.
20. Dibble, L. A., and Raupp, G. B., *Catal. Lett.* **4,** 345–354 (1990).
21. Dibble, L. A., and Raupp, G. B., *Environ. Sci. Technol.* **26,** 492–495 (1992).
22. Phillips, L. A., and Raupp, G. B., *J. Mol. Catal.* **77,** 297–311 (1992).
23. Jacoby, W. A., Ph.D. thesis, University of Colorado, 1993.
24. Nimlos, M. R., Jacoby, W. A., Blake, D. M., and Milne, T. A., *Environ. Sci. Technol.* **27,** 732–740 (1993).
25. Anderson, M. A., Yamazaki-Nishida, S., and Cervera-March, S., *in* "Proceedings, First International Conference on TiO_2 Photocatalytic Purification and Treatment of Water and Air, London, Ontario, Canada, 8–13 November 1992" (D. F. Olis and H. Al-Ekabi, Eds.), pp. 405–420, Elsevier, Amsterdam, 1993.
26. Holden, W., Marcellino, A., Valic, D., and Weedon, A. C., *in* "Proceedings, First International Conference on TiO_2 Photocatalytic Purification and Treatment of Water and Air, London, Ontario, Canada, 8–13 Nov. 1992," (D. F. Ollis and H. Al-Ekabi, Eds.), pp. 393–404. Elsevier, Amsterdam, 1993.
27. Yamazaki-Nishida, S., Nagano, K. J., Phillips, L. A., Cervera-March, S., and Anderson, M. A., *J. Photochem. Photobiol. A* **70,** 95–99 (1993).
28. Jacoby, W. A., Nimlos, M. R., and Blake, D. M., *Environ. Sci. Technol.* **28,** 1661–1668 (1994).
29. Larson, S. A., and Falconer, J. L., submitted.
30. Mozzanega, H., Herrmann, J.-M., and Pichat, P., *J. Phys. Chem.* **83**(17), 2251–2255 (1979).
31. Miller, R., and Fox, R., *in* "Proceedings, First International Conference on TiO_2 Photocatalytic Purification and Treatment of Water and Air, London, Ontario, Canada, 8–13 Nov. 1992" (D. F. Ollis and H. Al-Ekabi, Eds.), Elsevier, Amsterdam, 1993.
32. Wolfrum, E., Turchi, C., Bintner, G., and Nimlos, M., "The Fourth International Symposium on Chemical Oxidation: Technology for the Nineties, Vanderbilt University, Nashville, Tennessee, February 1994."
33. Heinsohn, R. J., "Industrial Ventilation Engineering Principles." Wiley, New York, 1991.
34. Irandoust, S., and Andersson, B., *Catal. Rev. Sci. Eng.* **30**(3), 341–392 (1988).
35. Votruba, J., Mikus, O., Hlavacek, V., and Skrivanek, J., *Chem. Eng. Sci.* **29,** 2128–2130 (1974).
36. Ollis, D. F., *in* "Proceedings, First International Conference on TiO_2 Photocatalytic Purification and Treatment of Water and Air, London, Ontario, Canada, 8–13 Nov. 1992" (D. F. Ollis and H. Al-Ekabi, eds.), pp. 481–494. Elsevier, Amsterdam, 1993.
37. Luo, Y., Ph.D. thesis, North Carolina State University (1994).
38. Berman, E., and Dong, J., *in* "The Third International Symposium Chemical Oxidation: Technology for the Nineties, Vanderbilt University, Nashville, TN, 1993" (W. W. Eckenfelder, A. R. Bowers, and J. A. Roth, Eds.), pp. 183–189. Technomic Publishing, 1993.
39. Sauer, M. L., and Ollis, D. F., submitted.
40. Sato, S., *J. Phys. Chem.* **87**(18), 3531–3537 (1983).
41. Wolfrum, E., NREL (personal communication), 1995.
42. Pruden, A. L., and Ollis, D. F., *J. Catal.* **82,** 404–417 (1983).
43. Turchi, C. S., and Ollis, D. F., *J. Catal.* **119,** 483–496 (1989).